

Mario Arroyo-Solórzano^{1,2}, Lucas Crisosto¹, Jorge Jara¹, Álvaro González³, and Fabrice Cotton^{1,2}

¹GFZ Helmholtz Centre for Geosciences

²Institute of Geosciences, University of Potsdam

³Departament de Dinàmica de la Terra i de l'Oceà, Universitat de Barcelona. Martí i Franqués

November 12, 2025

Abstract

Slow-slip events (SSEs) release tectonic stress aseismically along subduction interfaces at shallow (<20 km) and deep (30-60 km) depths. Here, we explore nonlinear relationships between subduction features (geometric, kinematic, and structural parameters) and the occurrence of SSEs, using two machine learning algorithms based on decision trees. Our results indicate that SSEs mainly occur in subduction interfaces with low dip angles, slow convergence, and heterogeneous or fluid-rich conditions. Shallow SSEs are further associated with slab roughness, erosive margins, and high lithostatic pressures, whereas deep SSEs mostly correlate to young slabs showing pronounced negative shear-wave velocity anomalies, and low lithostatic pressures. These patterns identify the most influential controls on shallow and deep SSEs, revealing a depth-dependent interplay among geometric, kinematic, and rheological factors. Our global model forecasts in which subduction margin SSEs are likely but remain undetected, offering a predictive framework for future monitoring of SSEs and their impact on hazard assessment.

1 **Subduction Parameters Controlling the Occurrence of Shallow and Deep Slow-Slip**
2 **Events (SSEs) Revealed by Machine Learning**

4 **Mario Arroyo-Solórzano^{1,2}, Lucas Crisosto¹, Jorge Jara¹, Álvaro González³ and Fabrice**
5 **Cotton^{1,2}**

6 ¹ GFZ Helmholtz Centre for Geosciences, Telegrafenberg, 14473 Potsdam, Germany.

7 ² Institute of Geosciences, University of Potsdam, 14476 Potsdam, Germany.

8 ³ Departament de Dinàmica de la Terra i de l'Oceà, Facultat de Ciències de la Terra, Universitat
9 de Barcelona. Martí i Franqués, 08028 Barcelona, Spain.

10 Corresponding author: Mario Arroyo-Solórzano (marroyo@gfz.de)

12 **Key Points:**

- 13 • Our results identify key factors controlling SSEs and forecast regions where they may exist
14 and remain undetected.
- 15 • SSEs occur mainly in regions with low dip angles, slow convergence, and heterogeneous
16 or fluid-rich conditions.
- 17 • Shallow SSEs are favored by rough, erosive, high-pressure margins, while deep SSEs by
18 young slabs with low lithostatic pressures.

20 **Abstract**

21 Slow-slip events (SSEs) release tectonic stress aseismically along subduction interfaces at shallow
22 (<20 km) and deep (30–60 km) depths. Here, we explore nonlinear relationships between
23 subduction features (geometric, kinematic, and structural parameters) and the occurrence of SSEs,
24 using two machine learning algorithms based on decision trees. Our results indicate that SSEs
25 mainly occur in subduction interfaces with low dip angles, slow convergence, and heterogeneous
26 or fluid-rich conditions. Shallow SSEs are further associated with slab roughness, erosive
27 margins, and high lithostatic pressures, whereas deep SSEs mostly correlate to young slabs
28 showing pronounced negative shear-wave velocity anomalies, and low lithostatic pressures. These
29 patterns identify the most influential controls on shallow and deep SSEs, revealing a depth-
30 dependent interplay among geometric, kinematic, and rheological factors. Our global model
31 forecasts in which subduction margins SSEs are likely but remain undetected, offering a predictive
32 framework for future monitoring of SSEs and their impact on hazard assessment.

33

34 **Plain Language Summary**

35 Slow-slip events are silent, slow movements of faults that release tectonic stress without generating
36 damaging earthquakes. It is important to understand why they occur because they may influence
37 where or when large earthquakes may happen. They have been detected at different depths of
38 subduction plate boundaries, where one tectonic plate slides beneath another. We here investigate
39 which properties of these boundaries control where such slow movements take place. For that, we
40 analyze the plates geometry, how quickly they move, how rough their contact is, among other
41 features. Using machine learning we discover which of these properties are present where such
42 slow events occur, unveiling hidden combinations of properties which would have been difficult
43 to notice with simpler techniques. Since instruments to detect these events are unevenly distributed
44 worldwide and especially scarce offshore, our results are important for forecasting where slow-
45 slip events may exist but remain undetected.

46

47 **1. Introduction**

48 Subduction zones host a continuum of slip behaviors, from great earthquakes ($M_w \geq 8.5$)
49 to slow, aseismic deformation along the plate interface. While the physical conditions favoring
50 giant earthquakes are well studied (Brizzi et al., 2018; Graciosa et al., 2025; Heuret et al., 2011,
51 2012; Lallemand et al., 2018; Locher et al., 2025; Muldashev & Sobolev, 2020), factors controlling
52 shallow and deep slow-slip events (SSEs) remain debated (Avouac, 2015; Barnes et al., 2020;
53 Bassett et al., 2025; Bürgmann, 2018; Im et al., 2020; McLellan & Audet, 2020). SSEs have been
54 reported in several subduction zones (Figure 1a), including Cascadia, Alaska, Mexico, Costa Rica,
55 Japan, New Zealand and South America (Dascher-Cousineau & Bürgmann, 2024; Kano et al.,
56 2018, and references therein). These events occur at shallow (<20 km) and deep (30–60 km)
57 depths, last from days to months, and release a significant fraction of tectonic strain (Jara et al.,
58 2024; Nishikawa et al., 2023; Wallace et al., 2016). Moreover, SSEs are also important as they
59 may precede major to moderate earthquakes (Caballero et al., 2021; Cruz-Atienza et al., 2021;
60 Socquet et al., 2017), and influence long-term seismic hazard (Arroyo-Solórzano et al., 2025;
61 Obara & Kato, 2016; Plata-Martinez et al., 2021).

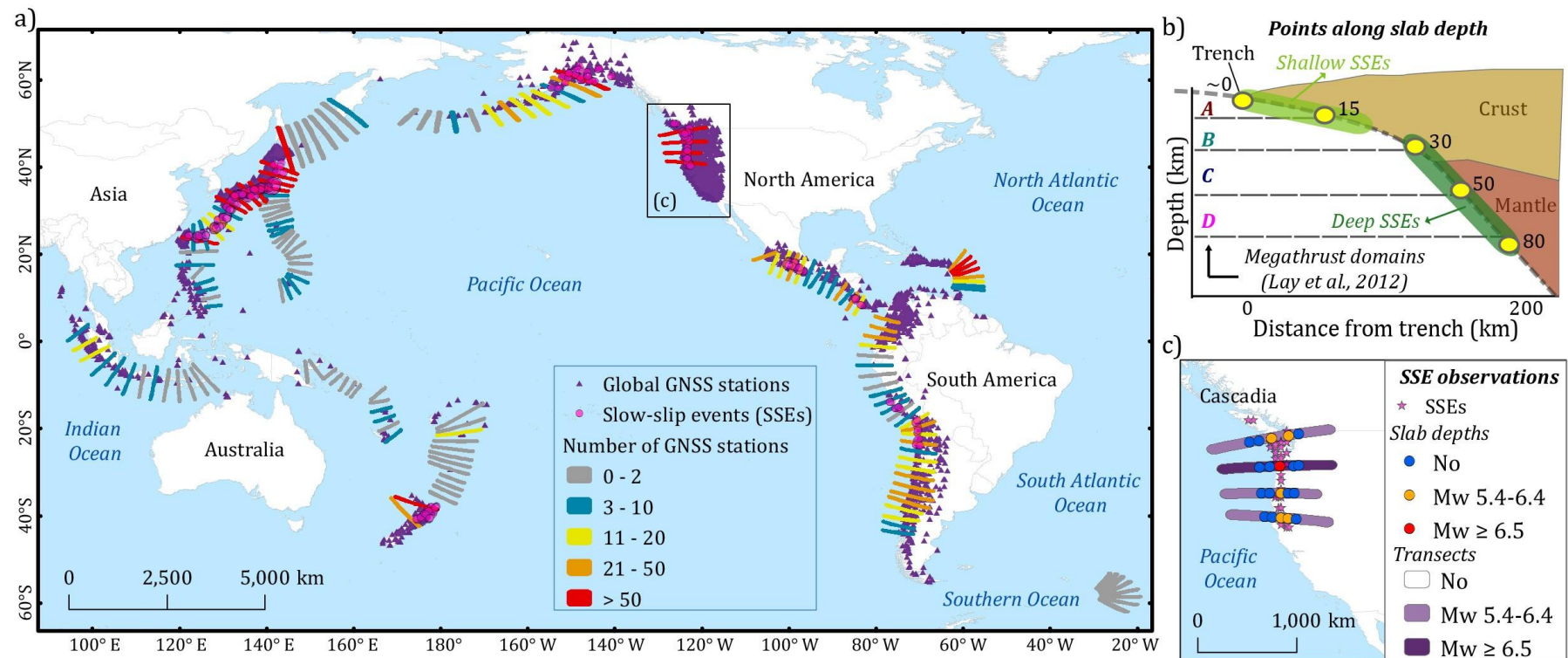


Figure 1. Global transect-based framework, GNSS coverage, and SSEs distribution along subduction zones. a) Spatial distribution of transects, colored by the number of GNSS stations within a 100 km buffer, based on the Nevada Geodetic Laboratory database (Blewitt et al., 2018). Only transects with at least three GNSS stations are included for machine learning analysis. b) Schematic representation of the evaluated points along each transect at different slab depths, with megathrust domains (A-D) following Lay et al. (2012). c) Example from the Cascadia margin showing the presence or absence of SSEs by transect and slab depths. Colors denote SSE magnitudes (M_w 5.4–6.4 and $M_w \geq 6.5$). Larger SSEs are assigned higher weights in the model (see Figure S2 in Supporting Information S1 for the global map of transects used and the SSEs magnitudes associated).

Conditions favoring the occurrence of SSEs at shallow and deep depths result from the combined influence of several interacting subduction parameters (Bassett et al., 2025). Overall, SSEs have been linked to near-lithostatic pore-fluid pressures, subducting seafloor roughness, and the presence of sediments and fluids along the subduction interface (Avouac, 2015; Bürgmann, 2018, and references therein). However, distinct mechanisms appear to dominate at different depths, reflecting variations in slip behavior along the megathrust (Lay et al., 2012). Shallow SSEs are typically associated with fluid overpressure, low effective stress, sediment lenses, and heterogeneous fault interfaces (Bangs et al., 2023; Barnes et al., 2020; Perez-Silva et al., 2022; Saffer & Wallace, 2015; Shreedharan et al., 2022). In contrast, deep SSEs occur under higher temperatures, with recurrence and duration modulated by interface geometry and rheology (Gao & Wang, 2017; Li & Liu, 2016; Perez-Silva et al., 2023). These observations are mostly based on qualitative studies from specific regions, underscoring the lack of global quantitative assessments of the key features controlling shallow and deep SSEs.

SSEs detection is also hampered by the uneven geodetic coverage (Blewitt et al., 2018, Figure 1a). That is, our observations are biased by which subduction margins are properly monitored, with insufficient geodetic coverage being particularly evident offshore (Ide & Beroza, 2023). To address this limitation, we compile a global dataset that integrates slab geometry, kinematics, and structural properties with SSE catalogs to evaluate the combined influence of such parameters (Text S1, Supporting Information S1). This dataset provides a consistent framework to explore quantitatively the physical settings that favor SSEs across subduction zones, assess their relative contributions, and identify potential biases arising from monitoring gaps.

We apply two supervised decision-tree-based machine-learning (ML) algorithms to capture nonlinear interactions among subduction parameters and determine the conditions under which SSEs occur. Similar analyses have been applied for short and long-term deep SSEs (McLellan & Audet, 2020), assessing the potential for giant earthquakes (Graciosa et al., 2025; Locher et al., 2025) and *b*-value variability (Crisosto & Tassara, 2024). Here, we assess whether SSEs can occur in any subduction zone or at specific depths, combining a systematic transect-based analysis (Figure 1a) covering most subduction zones, with a depth-dependent approach (Figure 1b) to evaluate slab-depth variations. We then apply explainability techniques to the outputs of the ML models to rank the importance and contributions of different features for shallow and deep SSEs. Finally, we infer SSEs potential, identifying regions where SSEs may exist but remain undetected.

2. Data and Methods

2.1 Dataset

To examine the potential for SSEs worldwide, we use 162 trench-perpendicular transects from Crisosto & Tassara (2024) and the Submap database (Lallemand & Heuret, 2017, <https://submap.fr>). These transects are globally spaced by ~2° along the trench axis (Figure 1a) where the Slab2.0 model is used as reference (Hayes et al., 2018). To examine depth-dependent variations, each transect is sampled at interface depths of 0, 15, 30, 50, and 80 km (Figure 1b), following the megathrust domains defined by Lay et al. (2012). This dual resolution (transects and slab depths) enables complementarity between large-scale subduction characteristics and local interface conditions.

We compiled a consistent global dataset of physical parameters to enable broad-scale analyses of subduction dynamics and potential controls on the occurrence of SSEs. Input features includes slab age (age), average dip angle (dip_avg), dip at slab depth (dip), convergence rate over the last 10 My (vc), current geodetic convergence rate (vcP), obliquity angles (obl_vc, obl_vcP), upper plate strain (ups), margin type (AvsE), trench roughness (rough), sediment thickness (t_sed), lithostatic pressure (LP), and the mean anomaly of shear wave velocities V_s (dVs). Each parameter is assigned to transects, slab-depth points, or both, depending on spatial resolution, and correlation analyses indicate that most features are weakly correlated, suggesting their potential unique contributions (Text and Table S1; Figure S1, Supporting Information S1).

SSEs are classified as present or absent based on global catalogs (Dascher-Cousineau & Bürgmann, 2024; Kano et al., 2018). At the transect level (Dataset S1), an SSE is considered present if it occurs within 100 km of the transect. At the slab-depth level (Dataset S2), SSEs are assigned to the nearest sampled depth within 30 km. Shallow SSEs correspond to depths <20 km, whereas deep SSEs correspond to ≥ 20 km (Figure 1b and 1c). This classification enables consistent global comparisons between observed SSEs and the physical properties of subduction interfaces.

2.2 Machine learning

To analyze the nonlinear relationships among subduction parameters and the occurrence of SSEs, we apply two supervised ML algorithms based on decision trees: *CatBoost* (Prokhorenkova et al., 2018) and *XGBoost* (Chen & Guestrin, 2016). These models capture complex feature interactions and provide robust performance for relatively small and imbalanced datasets (Text S2, Supporting Information S1). Previous geophysical studies have shown that nonlinear tree-based classifiers consistently achieve strong predictive performance in similar contexts (Crisosto & Tassara, 2024; McLellan & Audet, 2020). In addition, we select *CatBoost* and *XGBoost* because their boosting techniques enhance predictive accuracy and model interpretability compared to standard ensemble methods such as *Random Forest* (Breiman, 2001).

We assign input parameters to each transect and slab-depth point, standardized, and encoded to ensure consistent training of the ML models (e.g., ups, AvsE, SSEs). To guarantee data quality, we retain only transects with at least three Global Navigation Satellite System (GNSS) stations within a 100 km buffer (Figure 1a), which represents the minimum observational density where SSEs have been reliably detected. Based on this criterion, 98 transects are selected and the presence/absence proportion for shallow SSEs is 74/24, whereas for deep SSEs is 64/34. Additionally, we apply a weighting scheme based on the number of stations in each transect (Figure 1a) using a logarithmic transformation normalized to [0.5, 1], and doubling the weight for SSEs with $M_w \geq 6.5$ (Figure 1c and Figure S2, Supporting Information S1).

To optimize model performance with the limited and imbalanced dataset, we tune hyperparameters through a randomized search using 4-fold cross-validation and a class-balance scaling factor (Probst et al., 2019; Zou et al., 2022). Then, we evaluate the models using stratified 10-fold and 5-fold cross-validation exploring train/test partitions of 90/10 and 80/20 per fold, respectively. In each fold, predictions are calibrated using isotonic regression to refine probability estimates. Next, the final performance metrics (accuracy, F1 score, ROC-AUC, and log-loss), are averaged across folds to provide robust estimates of models performance (Carrington et al., 2021). Finally, we apply the *SHAP* value method (Lundberg & Lee, 2017) to the best-performing model (Text S2 and Figure S3, Supporting Information S1). This approach allows us to quantify the contribution and influence of each feature on the presence or absence of SSEs.

156 **3. Results**

157 In this section, we focus on ML models interpretation, with summary metrics, ROC-AUC
 158 curves and confusion matrices provided in the Supporting Information (Tables S2 and S3; Figures
 159 S4 and S5). Our models consistently indicates that 10-fold cross-validation provides the best
 160 performance metrics, with *CatBoost* generally yielding the highest predictive performance, except
 161 for shallow SSEs at slab-depths, where *XGBoost* performs slightly better. This trend is possibly
 162 due to differences in handling categorical inputs (e.g., ups and AvsE; (Prokhorenkova et al., 2018)).
 163 We analyze our best models using *SHAP* (Lundberg & Lee, 2017) to rank features and quantify
 164 their effects on the probability of shallow and deep SSEs. Finally, we combine transect- and slab-
 165 depth-based probabilities into a weighted mean to integrate large-scale tectonic conditions with
 166 local variations, generating global maps of inferred SSEs potential.

167 **3.1.Shallow SSEs**

168 At the transect scale (Figure 2a), the average dip angle (dip_avg) emerges as the primary
 169 control on shallow SSEs, followed by the shear-wave velocity anomaly (dVs), roughness (rough),
 170 and margin type (AvsE). All other features are complementary or less relevant. Feature effects on
 171 model predictions show clear patterns, such as a negative correlation with dip_avg and dVs,
 172 indicating that low dip angles and negative velocity anomalies favor shallow SSEs. In contrast,
 173 rough and AvsE show a positive correlation, with most high values associated with shallow SSE.
 174 Complementary features show weak or inconsistent relations. These patterns are consistent with
 175 exploratory analysis showing that low dip angles ($dip_avg < 15^\circ$), V_s anomalies ($dVs < -1.0\%$),
 176 and roughness (> 100 m) correspond to higher probabilities of shallow SSEs (Figure S6,
 177 Supporting Information S1).

178 At slab-depth scale (Figure 2b), current convergence velocity (vcP) is the primary control
 179 on the occurrence of shallow SSEs, followed by lithostatic pressure (LP), V_s anomaly (dVs), and
 180 dip angle (dip). While depth-specific correlations for dVs are less consistent than at the transect
 181 level, positive anomalies generally inhibit shallow SSEs. Higher lithostatic pressures clearly
 182 correspond to higher predicted probabilities of shallow SSEs. No clear trends are observed for dip
 183 and vcP, and correlations for complementary features remain weak. Further exploratory analysis
 184 shows that shallow SSEs tend to occur at lower convergence velocities ($\sim 2\text{--}6$ cm/year), while LP
 185 values of 300–400 MPa correspond to larger shallow SSEs, consistent with the positive correlation
 186 between LP and shallow SSEs (Figure S7, Supporting Information S1).

187 **3.2.Deep SSEs**

188 The transect-level analysis (Figure 2c) identifies convergence velocity (vc), average dip
 189 angle (dip_avg), and V_s anomaly (dVs) as primary factors controlling deep SSEs. Feature trends
 190 show no clear correlation between vc and deep SSEs, whereas lower values of dip_avg and dVs
 191 favor their occurrence. The obliquity angle of vc (obl_vc) and slab age at the trench (age) act as
 192 secondary parameters, where obl_vc do not show a clear correlation with deep SSEs, while
 193 younger slab ages are associated with deep SSEs. Remaining features are complementary, with
 194 AvsE and roughness showing similar trends to shallow SSEs but with lower relevance, indicating
 195 a reduced influence on SSEs deeper than 20 km. Exploratory analysis supports these findings,
 196 showing overlap in vc values between regions with and without deep SSEs, while dip_avg $< 20^\circ$,
 197 dVs $< -1\%$, and age < 60 My correspond to conditions prone to deep SSEs (Figure S8, Supporting
 198 Information S1).

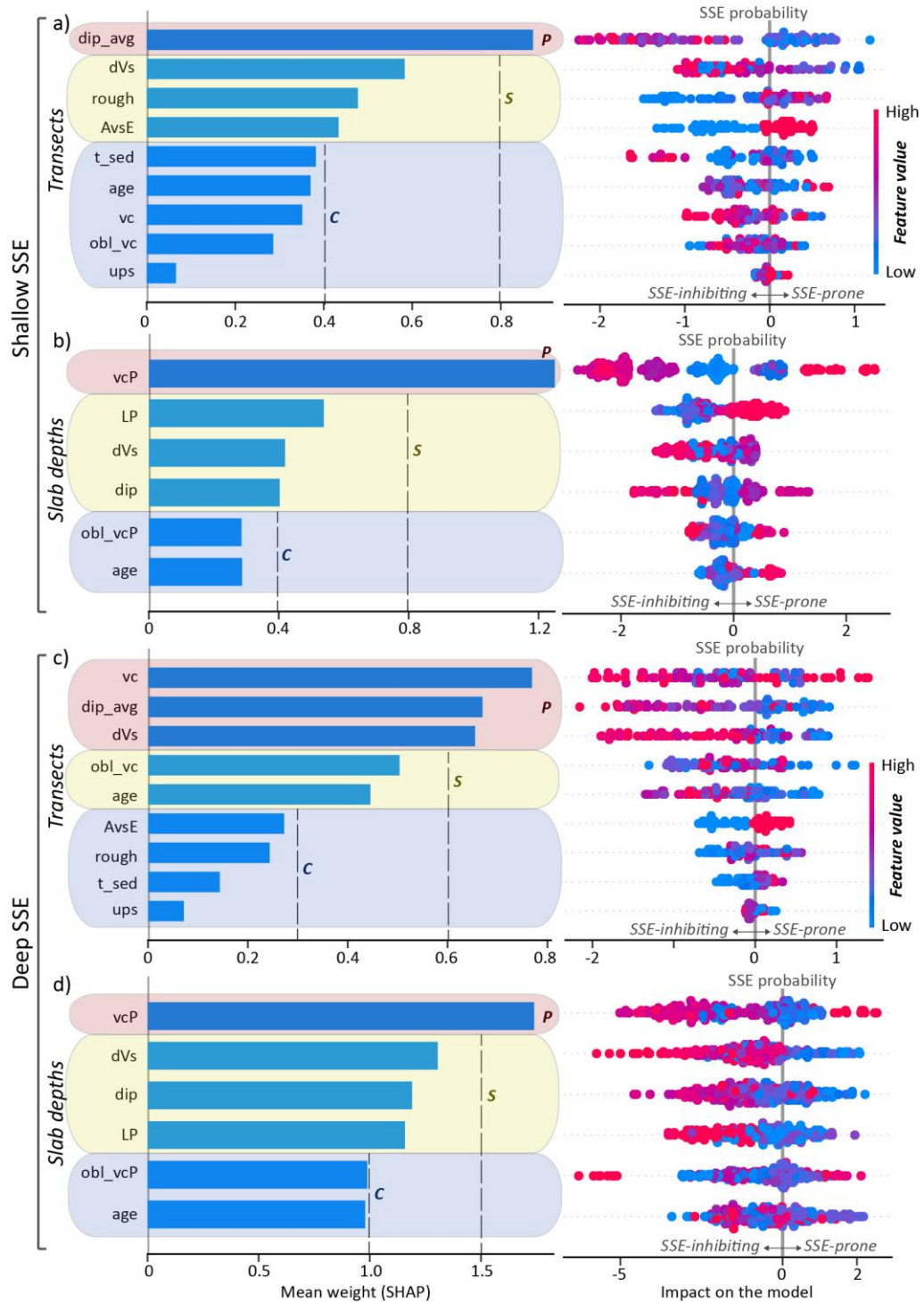


Figure 2. SHAP-based relevance of features controlling shallow and deep SSEs. (a–b) Shallow SSEs by transect and slab depth. (c–d) Deep SSEs by transect and slab depth. Left panels show the mean SHAP weights ranking each feature by its relative contribution to the model. Right panels display their effect on model predictions, where positive values increase and negative values decrease SSEs probability. P, S, and C denote Primary, Secondary, and Complementary features. Feature acronyms: age (slab age), dip_avg (average dip angle), dip (local dip), vc (10 My convergence velocity), vcP (current convergence velocity), obl_vc / obl_vcP (obliquity angles), ups (upper-plate strain), AvsE (margin type), rough (roughness), t_sed (trench sediments), LP (lithostatic pressure), and dVs (V_s anomaly).

At slab-depth scale (Figure 2d), the feature ranking for deep SSEs is similar to shallow. Current convergence velocities (v_{CP}) is the primary factor, and unlike in shallow SSEs, the trend is clear, with high v_{CP} values inhibiting, while low values promote deep SSE. Secondary features are the same as for shallow SSEs but ranked as dVs, dip, and LP. The trends for dVs and dip are stronger than for shallow SSEs and consistent with the transect-level analysis: lower values favoring deep SSEs. In contrast, LP shows an inverse correlation compared to shallow SSEs, where in this case lower lithostatic pressures at depths greater than 20 km promote their occurrence. Correlations for complementary features remain weak, although their relative contribution is higher than for shallow SSEs. Model outcomes are further supported by the exploratory analysis, showing deep SSEs occur mostly where there are low values of v_{CP} (~2–5 cm/year), dip angle (< 25°), dVs (< -1%), and LP (1000–1500 MPa) (Figure S9, Supporting Information S1).

3.3. Probabilistic Inferences of SSEs

We combine transect- and slab-depth-based probabilities into a weighted mean to infer the global potential for SSEs. This weighting scheme assigns equal contributions to both approaches (0.5 transect, 0.5 slab depth) to balance the higher predictive performance of the transect-based models with the broader depth coverage of the slab-depth analysis (Figure S10, Supporting Information S1). Four potential categories are defined from the combined probability distribution (Figure 3): very high (>50%), high (20–50%), moderate (5–20%), and low (<5%), with thresholds based on probability density distributions of the combined weights (Figure S11, Supporting Information S1). The resulting SSEs inference map indicates that most slab depths (~75–80%) have at least moderate potential, and nearly all subduction zones could host SSEs at specific depths (Figure 3).

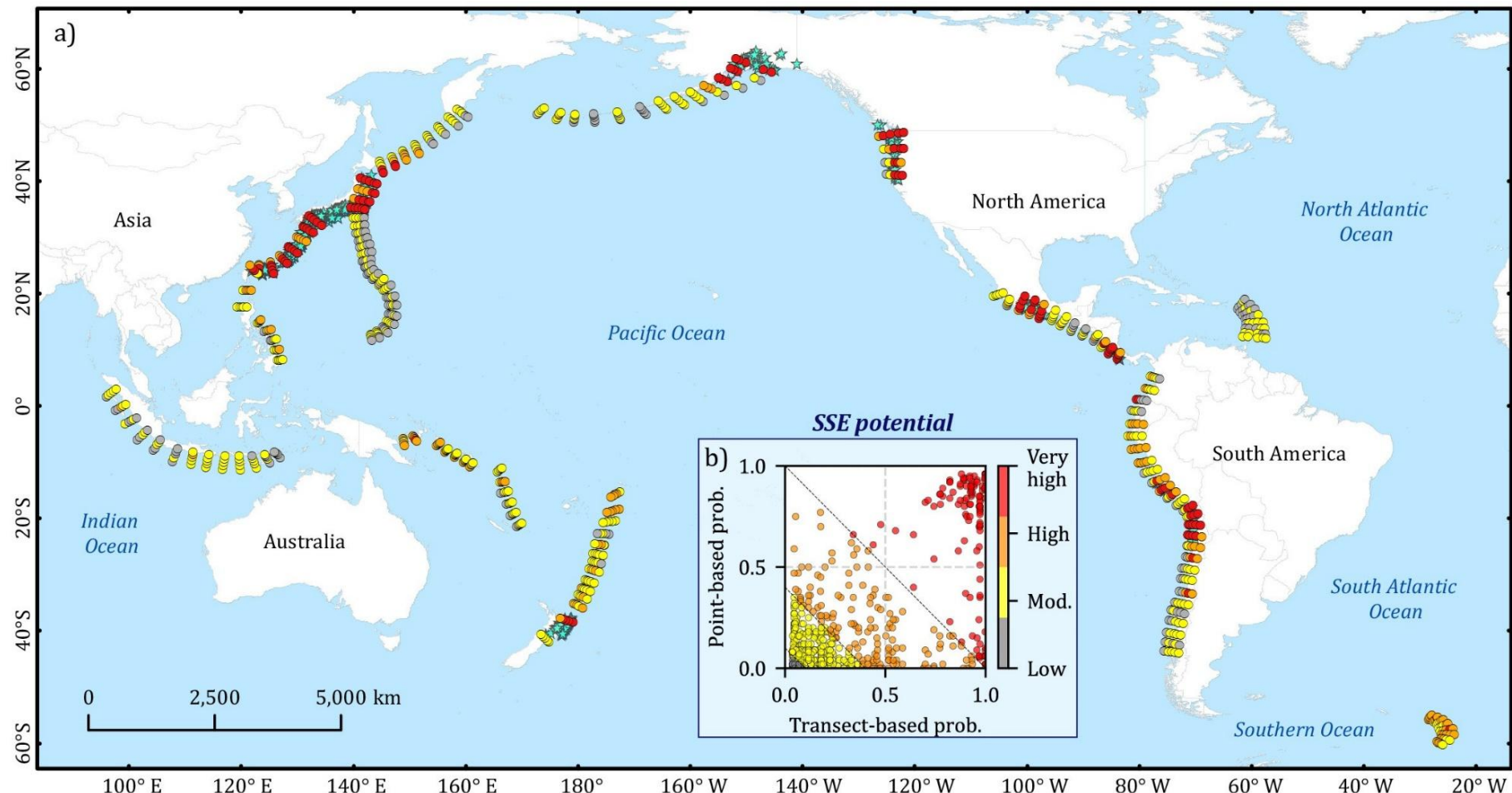
To explore the consistency between our SSEs potential classification and observed events, we examine category distributions across four paired-variable plots, considering v_{CP} , dVs, LP, dip, and slab age (Figure 4a–4d). All plots show positive correlations with observed SSEs, with larger clusters at low values for most features, consistent with our ML interpretations (Figure 4f), and remarking low v_{CP} (2–6 cm/year), dip (< 25°), dVs (< -1%), and age (< 60 My) as the settings most prone to SSEs (Figure 2). For LP, 0.3–1.5 GPa stands out as most favorable (Figure 4c), with higher LP favoring shallower SSEs and lower LP favoring deeper SSEs (Figures 2c–2d and 4f). Additionally, violin plots of slab depths (Figure 4e) further confirm that high and very high potential closely aligns with observed SSEs, confirming model consistency.

4. Discussion

4.1. SSEs Depth-Dependence

We find the occurrence of SSEs primarily controlled by low dip angles, slow convergence rates, and negative V_s anomalies (Figure 4f). We associate their influence with low dip angles reducing frictional resistance (Bassett et al., 2025; Li & Liu, 2016; Perez-Silva et al., 2022), slow convergence rates generating instabilities near the transition between rate-weakening and rate-strengthening regimes (Im et al., 2020; Mei & Wang, 2024; Perez-Silva et al., 2023), and negative V_s anomalies indicating zones with high geological heterogeneity or partial melting creating fluid-rich conditions (Lu et al., 2019; Wada & Wang, 2009). Together, these factors increase pore pressure and lower effective normal stress, facilitating episodic SSEs along the interface (Bürgmann, 2018).

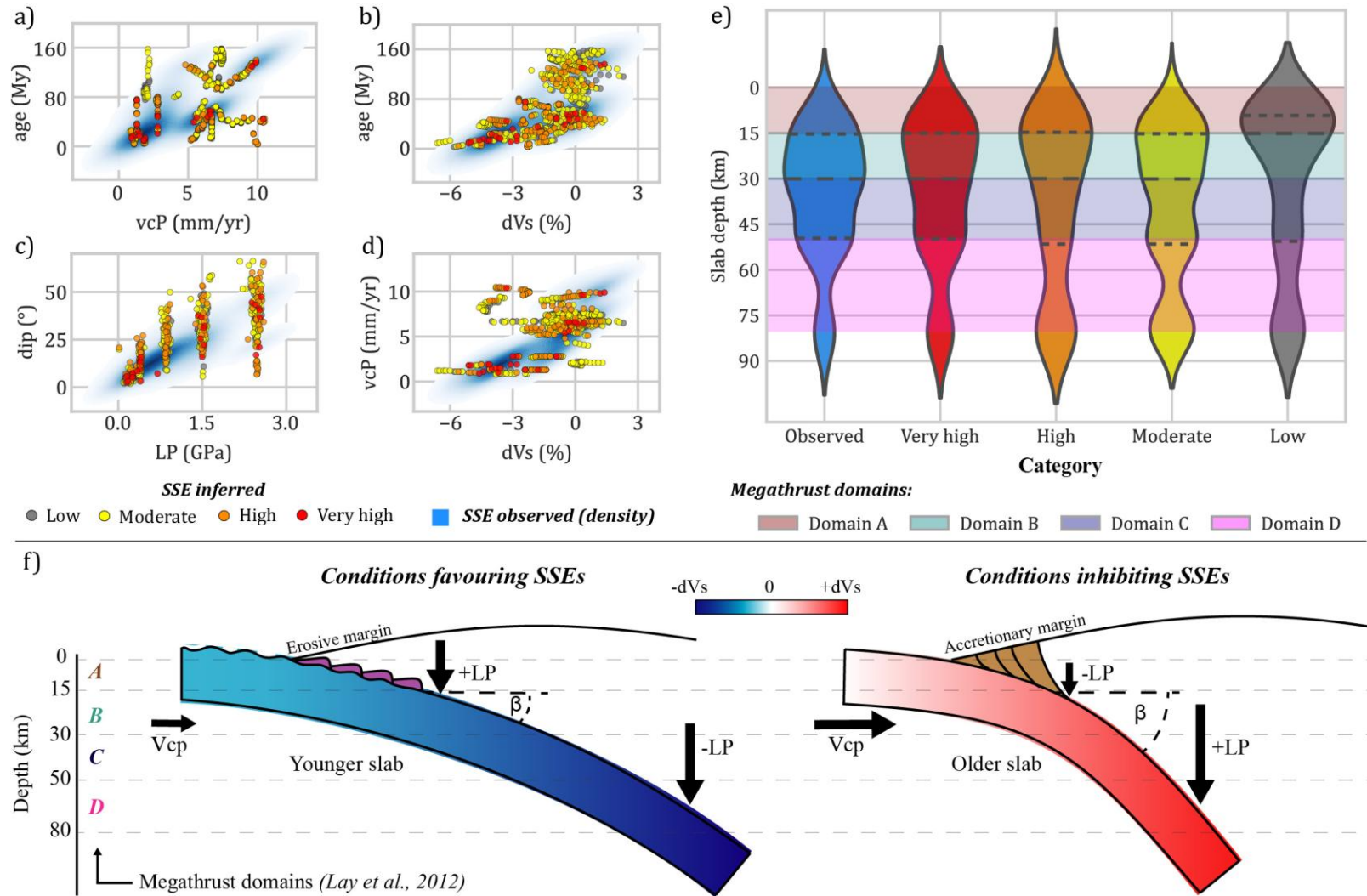
250



251

252
253
254
255

Figure 3. SSEs inference map and probability plot. a) SSE potential inferred from the weighted combination (0.5 transect-based and 0.5 slab-depth-based probabilities). Stars mark locations of observed SSEs from the global catalog, and in them the potential is not forecast, since they are model inputs. b) Probability plot showing the classification of SSE potential into very high, high, moderate, and low categories (see Figure S10 in Supporting Information S1 for separate classifications based on transect- and slab-depth analyses).



256

257

258

259

260

261

Figure 4. Comparison of inferred and observed SSEs, and conceptual model of conditions favoring or inhibiting SSEs. Evaluation of key feature pairs: a) current velocity of convergence (vcP) vs. age; b) percentage anomaly of Vs (dVs) vs. age; c) lithostatic pressure (LP) vs. dip; d) percentage anomaly of V_s (dVs) vs. current velocity of convergence (vcP). e) Violin plots showing slab depths for observed SSE and potential model-based categories. f) Conceptual model summarizing conditions favoring or inhibiting SSEs. Lower and higher dip angles are indicated as β . Magnitudes of vcP and LP are shown as arrows size. Shaded regions (e) and letters (f) indicate megathrust domains (Lay et al., 2012).

Shallow and deep SSEs show distinct patterns shaped by additional depth-dependent factors (Figures 2a-2d and 4f). Shallow SSEs are promoted by high roughness, erosive margins, and high lithostatic pressures compared to other regions at similar depths (< 20 km). In contrast, deep SSEs occur preferentially in young slabs, in regions characterized by stronger negative dVs anomalies and relative low lithostatic pressures compared to other regions at similar depths (> 20 km). For shallow SSEs, we relate the combined effect of interface roughness and margin type with creep generation, where the former induces stress through geometric heterogeneity (Avouac, 2015; Wang & Bilek, 2014), and the latter limits sediment accumulation, maintaining slip heterogeneities and reducing coupling along the interface (Heuret et al., 2012). For deep SSEs, we link younger slab ages and stronger negative V_s anomalies with warm subduction zones characterized by higher slab thermal states that may facilitate fluid overpressure in semi-ductile regions and metamorphism (Gao & Wang, 2017; McLellan & Audet, 2020). Finally, the combined effects of lithostatic pressure, dip, dVs, and other key parameters (Figures 2b, 2d and 4f), create thermal and fluid-rich conditions that promote SSEs in transitional frictional regimes between the seismogenic zone and deeper tremor areas (Behr & Bürgmann, 2021; Shreedharan et al., 2022).

McLellan & Audet (2020) analyzed deep short- and long-term SSEs, evaluating dip angles, convergence velocities, sediments, roughness, and slab ages. They found young ages and slow convergences as the most relevant for short-term SSEs, whereas for long-term events, low dip angles and slow convergences dominate. In their results, roughness appears irrelevant in both cases, consistent with our finding that it plays a minor role for deep SSEs. However, for shallow SSEs, in our model roughness is a relevant factor (Figures 2a and 4f). This influence of roughness on favouring SSEs may arise from the interaction with other features. For instance, connections between subducted seamounts and sediments, where material trapped behind seamounts increases pore pressure and reduces effective normal stress, whereas sediments overlying seamounts smooth the interface, reducing heterogeneity and suppressing SSEs (Bangs et al., 2023). This idea also align well with our results, where trench sediments (t_{sed}) have little influence on SSEs (Figure 2a and 2c), likely due to loss or lithification during subduction that smooths the interface.

Lay et al. (2012) divide the megathrust into four depth domains and associate SSEs mainly with domains A and D (Figures 1b and 4f). We instead find that observed SSEs and high-potential areas commonly occur within transition zones (A-B, B-C, and C-D; Figure 4e), suggesting the presence of SSEs within the megathrust seismogenic zone, likely adjacent to locked patches (Peng & Gomberg, 2010). Additionally, long-term SSEs occurring up-dip of short-term events have been linked to pressure and temperature conditions that generate semi-frictional or viscous behaviour (Gao & Wang, 2017; Perez-Silva et al., 2023). The transitions observed (Figure 4e) indicate that such conditions may develop along the interface, generating spatial continuity between deep and shallow SSEs, with long-term events likely developing where SSEs migrate toward shallower depths (Jiang et al., 2017; Wallace et al., 2012). These patterns highlights variations in interface rigidity likely due to thermo-petrology conditions (Gao & Wang, 2017), and stress shifts from velocity-weakening to velocity-strengthening, generating frictionally unstable settings favorable for SSEs (Im et al., 2020; Mei & Wang, 2024; Perez-Silva et al., 2022).

4.2. Are SSEs Ubiquitous? Implications of the Inferred Potential

Our results indicate favorable conditions for SSEs across a wide range of subduction zones and depths. Low SSEs potential mainly clusters along the shallow interface (Figure 4e), consistent with the global predominance of deep over shallow SSEs. However, our model also suggests high

306 SSEs potential in shallow regions without reported events (Figure 3a), indicating that suitable
 307 physical conditions may exist in more areas than currently observed (Ide & Beroza, 2023; Jolivet
 308 & Frank, 2020). This observation highlights monitoring limitations due to sparse offshore geodetic
 309 coverage (Blewitt et al., 2018; Saffer & Wallace, 2015), and the potential presence of SSEs hidden
 310 within geodetic noise (Ide & Beroza, 2023; Jara et al., 2024).

311 High and very high SSEs potentials are forecast near locations where these events have
 312 been reported, indicating model consistency. These areas include Alaska, Japan, Cascadia, New
 313 Zealand, Mexico, Costa Rica, and the Central Andes (Figure 3a). In these regions, distinguishing
 314 between shallow and deep SSEs is particularly informative, revealing depths where SSEs have not
 315 yet been observed. For instance, in northern Cascadia, although only deep SSEs have been reported
 316 (Li & Liu, 2016), our results indicate high potential for shallow SSEs, in agreement with low-
 317 frequency earthquakes (LFEs) and tremors observed offshore (Chaudhuri & Ghosh, 2022), which
 318 are commonly associated with SSEs (Behr & Bürgmann, 2021). Similarly, in southern Costa Rica,
 319 high SSE potential is inferred at depths greater than those of recorded events (Perry et al., 2023),
 320 where tremors and LFEs have also been reported (Brown et al., 2009).

321 However, we also find high SSEs potential in regions without reported events (Figure 3a),
 322 indicating that the framework used is robust enough to extend the forecast beyond the available
 323 observations. These additional regions include northwest and central Java (Indonesia), shallow
 324 portions of the Kuril Islands, deeper sections in the western Aleutians, the Philippines, the Tonga-
 325 Kermadec subduction zone, and the northeast of New Zealand. In South America, we obtain high
 326 potential for shallow SSEs in Colombia, Peru and northern Chile, whereas deeper SSEs are favored
 327 further south in Chile, and the Sandwich Islands. Despite the lack of recorded SSEs, in several of
 328 these regions LFEs, tremors, repeaters, and swarms have been observed (Brown et al., 2009;
 329 Igarashi & Kato, 2021; Kano et al., 2018; Sáez et al., 2019), demonstrating a high likelihood of
 330 SSEs due to their association with these features (Behr & Bürgmann, 2021; Obara & Kato, 2016).

331 This forecast is independently testable because SSEs not included in our dataset could
 332 eventually serve as independent observations for comparison. For example, shallow SSEs were
 333 recently recorded northeast of the Japan subduction zone near the Kuril Islands (Okada &
 334 Nishimura, 2025) and in the Copiapó region, northern Chile (Münchmeyer et al., 2025). These
 335 events had not been yet included in our datasets, and, in both cases, our model forecasts high or
 336 very high potential for shallow SSEs (Figure 3a), supporting the reliability of the model. Our
 337 inferences also highlight regions of predominantly low SSEs potential, including northern Central
 338 America and the Caribbean, southernmost Chile, the Marianas Trench, and parts of Indonesia
 339 (Figure 3a). These results do not entirely exclude the presence of SSEs in these regions but indicate
 340 a considerably lower probability, particularly for SSEs with $M_w > 5.5$.

341 We provide new insights into identifying regions most prone to SSEs, which is highly
 342 relevant as these events can significantly influence seismic hazard. Previous studies have shown
 343 that incorporating SSEs into probabilistic seismic hazard assessments can substantially modify
 344 hazard estimates in some regions, such as Costa Rica (Arroyo-Solórzano et al., 2025). In addition,
 345 SSEs migration has also been linked to the nucleation of large earthquakes in Japan, Mexico, and
 346 Chile (Cruz-Atienza et al., 2021; Nishikawa et al., 2023; Socquet et al., 2017). Moreover, recent
 347 evidence indicates that seismicity rates are on average ~24% higher during SSEs than background
 348 levels (Dascher-Cousineau & Bürgmann, 2024). Therefore, identifying regions prone to SSEs is
 349 also essential to enhance short and long-term seismic hazard assessments.

350 **5. Conclusions**

351 Our results reveal key controls on shallow and deep SSEs and remark the depth-dependent
 352 interplay of physical patterns leading their occurrence. Nearly all subduction zones show at least
 353 moderate SSEs potential, indicating that favorable physical conditions are widespread. Both
 354 shallow and deep SSEs are primarily associated with low dip angles, slow convergence rates, and
 355 negative V_s anomalies, emphasizing the key role of geometric, kinematic, and rheological
 356 conditions along the plate interface. In addition, shallow SSEs are particularly promoted by
 357 interface roughness, erosive margins, and relatively high lithostatic pressures for these depths,
 358 whereas deep SSEs are favored by young slab age, more negative V_s anomalies and relatively
 359 lower lithostatic pressures for their respective depths.

360 We also present a comprehensive and adaptable dataset compilation that serves as a robust
 361 foundation for global studies of subduction dynamics. Although inherent limitations on features
 362 resolution and data extent, the inferred patterns reveal clear hierarchies and trends, outlining
 363 regions more prone to shallow, deep, or both types of SSEs. Our model captures both regional and
 364 local controls and may guide future monitoring and detection efforts. The global map of forecast
 365 SSEs potential is consistent with observed events and associated features (e.g., tremors and low-
 366 frequency earthquakes), highlighting regions where SSEs likely occur but remain undocumented
 367 due to sparse instrumentation, especially offshore. These findings provide a predictive framework
 368 to guide future monitoring of SSEs and improve the integration of these events on seismic hazard
 369 assessments.

370 **Acknowledgments**

371 M. Arroyo-Solórzano acknowledges the funding program number 57645448 from the
 372 Deutscher Akademischer Austauschdienst (DAAD). L. Crisosto acknowledges the National
 373 Agency for Research and Development (ANID), scholarship program: Becas Chile ANID-DAAD
 374 2025 (no. 57752768). J. Jara acknowledges partial funding from the Marie Skłodowska-Curie
 375 Postdoctoral Fellowship (grant no. 101066069) and the Volkswagen Foundation (grant no.
 376 0200087-00). Á. González is a Serra Húnter Fellow, supported by the grant PID2021-125979OB-
 377 I00 financed by the Spanish State Research Agency (MICIU/AEI /10.13039/501100011033) and
 378 FEDER (European Union).

379 Special thanks are due to Dr. Anne Socquet and Dr. Ángela M. Gómez-García for their
 380 suggestions and valuable feedback. We also thank Dr. Corne Kreemer, Dr. Francesca Funicello
 381 and Dr. Slvia Brizzi for their helpful clarifications on some queries about datasources used for the
 382 analysis and datasets compilation.

383 **Author contributions**

384 M. Arroyo-Solórzano designed the study, processed the data, made the figures and wrote
 385 the paper with contributions from all co-authors. All the authors interpreted, discussed, and
 386 analyzed the results and revised the article. The authors also acknowledge that there are no
 387 conflicts of interest recorded.

388 **Data Availability Statement**

389 GNSS stations location were obtained from the Nevada Geodetic Laboratory:
 390 <https://geodesy.unr.edu/NGLStationPages/llh.out>. Datasets and additional information on input

391 features, machine learning related methods, and complementary figures are available as
 392 Supporting Information to complement the main article and provide readers with an open review
 393 of the analysis performed. All plots and figures were created using Python codes, Adobe Illustrator,
 394 and ArcMap.
 395

396 References

- 397 Arroyo-Solórzano, M., Jara, J., Weatherill, G., González, Á., Hidalgo-Leiva, D. A., & Cotton, F. (2025). Impact of
 398 geodetic information, subduction zone segmentation, and slow-slip events in probabilistic seismic hazard: A
 399 case study for Costa Rica. *Geophysical Journal International*, 242, 1–33. <https://doi.org/10.1093/gji/ggaf204>
- 400 Avouac, J. P. (2015). From geodetic imaging of seismic and aseismic fault slip to dynamic modeling of the seismic
 401 cycle. *Annual Review of Earth and Planetary Sciences*, 43, 233–271. <https://doi.org/10.1146/annurev-earth-060614-105302>
- 403 Bangs, N. L., Morgan, J. K., Bell, R. E., Han, S., Arai, R., Kodaira, S., et al. (2023). Slow slip along the Hikurangi
 404 margin linked to fluid-rich sediments trailing subducting seamounts. *Nature Geoscience*, 16(6), 505–512.
 405 <https://doi.org/10.1038/s41561-023-01186-3>
- 406 Barnes, P. M., Wallace, L. M., Saffer, D. M., Bell, R. E., Underwood, M. B., Fagereng, A., et al. (2020). Slow slip
 407 source characterized by lithological and geometric heterogeneity. *Sci. Adv.*, 6.
 408 <https://doi.org/10.1126/sciadv.aay3314>
- 409 Bassett, D., Shillington, D. J., Wallace, L. M., & Elliott, J. L. (2025). Variation in slip behaviour along megathrusts
 410 controlled by multiple physical properties. *Nature Geoscience*, 18(1), 20–31. <https://doi.org/10.1038/s41561-024-01617-9>
- 412 Behr, W. M., & Bürgmann, R. (2021). What's down there? The structures, materials and environment of deep-
 413 seated slow slip and tremor. *Philosophical Transactions of the Royal Society A: Mathematical, Physical and
 414 Engineering Sciences*, 379(2193). <https://doi.org/10.1098/rsta.2020.0218>
- 415 Blewitt, G., Hammond, W., & Kreemer, C. (2018). Harnessing the GPS data explosion for interdisciplinary science.
 416 *Eos*, 99. <https://doi.org/10.1029/2018EO104623>
- 417 Breiman, L. (2001). Random Forests. *Machine Learning*, 45, 5–32.
- 418 Brizzi, S., Sandri, L., Funiciello, F., Corbi, F., Piromallo, C., & Heuret, A. (2018). Multivariate statistical analysis to
 419 investigate the subduction zone parameters favoring the occurrence of giant megathrust earthquakes.
 420 *Tectonophysics*, 728–729, 92–103. <https://doi.org/10.1016/j.tecto.2018.01.027>
- 421 Brown, J. R., Beroza, G. C., Ide, S., Ohta, K., Shelly, D. R., Schwartz, S. Y., et al. (2009). Deep low-frequency
 422 earthquakes in tremor localize to the plate interface in multiple subduction zones. *Geophysical Research
 423 Letters*, 36(19). <https://doi.org/10.1029/2009GL040027>
- 424 Bürgmann, R. (2018). The geophysics, geology and mechanics of slow fault slip. *Earth and Planetary Science
 425 Letters*, 495, 112–134. <https://doi.org/10.1016/j.epsl.2018.04.062>
- 426 Caballero, E., Chouimet, A., Duputel, Z., Jara, J., Twardzik, C., & Jolivet, R. (2021). Seismic and Aseismic Fault Slip
 427 During the Initiation Phase of the 2017 MW = 6.9 Valparaíso Earthquake. *Geophysical Research Letters*,
 428 48(6). <https://doi.org/10.1029/2020GL091916>
- 429 Carrington, A. M., Manuel, D. G., Fieguth, P. W., Ramsay, T., Osmani, V., Wernly, B., et al. (2021). Deep ROC
 430 Analysis and AUC as Balanced Average Accuracy to Improve Model Selection, Understanding and
 431 Interpretation. *IEEE Transactions on Pattern Analysis and Machine Intelligence*.
 432 <https://doi.org/10.1109/TPAMI.2022.3145392>
- 433 Chaudhuri, K., & Ghosh, A. (2022). Widespread Very Low Frequency Earthquakes (VLFEs) Activity Offshore
 434 Cascadia. *Geophysical Research Letters*, 49(13). <https://doi.org/10.1029/2022GL097962>
- 435 Chen, T., & Guestrin, C. (2016). XGBoost: A scalable tree boosting system. In *Proceedings of the ACM SIGKDD
 436 International Conference on Knowledge Discovery and Data Mining* (Vol. 13-17-August-2016, pp. 785–794).
 437 Association for Computing Machinery. <https://doi.org/10.1145/2939672.2939785>
- 438 Crisosto, L., & Tassara, A. (2024). Relating Megathrust Seismogenic Behavior and Subduction Parameters via
 439 Machine Learning at Global Scale. *Geophysical Research Letters*, 51(20).
 440 <https://doi.org/10.1029/2024GL110984>
- 441 Cruz-Atienza, V. M., Tago, J., Villafuerte, C., Wei, M., Garza-Girón, R., Dominguez, L. A., et al. (2021). Short-
 442 term interaction between silent and devastating earthquakes in Mexico. *Nature Communications*, 12(1).
 443 <https://doi.org/10.1038/s41467-021-22326-6>

- 444 Dascher-Cousineau, K., & Bürgmann, R. (2024). Global subduction slow slip events and associated earthquakes.
 445 *Sci. Adv.*, 10, 2191. <https://doi.org/10.1126/sciadv.ado21>
- 446 Gao, X., & Wang, K. (2017). Rheological separation of the megathrust seismogenic zone and episodic tremor and
 447 slip. *Nature*, 543(7645), 416–419. <https://doi.org/10.1038/nature21389>
- 448 Graciosa, J. C., Capitanio, F. A., Beall, A., Hargreaves, M., Gollapalli, T., Tang, T., & Zuhair, M. (2025). Testing
 449 Driving Mechanisms of Megathrust Seismicity With Explainable Artificial Intelligence. *Journal of*
 450 *Geophysical Research: Solid Earth*, 130(1). <https://doi.org/10.1029/2024JB028774>
- 451 Hayes, G. P., Moore, G. L., Portner, D. E., Hearne, M., Flamme, H., Furtney, M., & Smoczyk, G. M. (2018). Slab2,
 452 a comprehensive subduction zone geometry model. *Science*, 362(6410), 58–61.
 453 <https://doi.org/10.1126/science.aat4723>
- 454 Heuret, Lallemand, S., Funiciello, F., Piromallo, C., & Faccenna, C. (2011). Physical characteristics of subduction
 455 interface type seismogenic zones revisited. *Geochemistry, Geophysics, Geosystems*, 12(1).
 456 <https://doi.org/10.1029/2010GC003230>
- 457 Heuret, Conrad, C. P., Funiciello, F., Lallemand, S., & Sandri, L. (2012). Relation between subduction megathrust
 458 earthquakes, trench sediment thickness and upper plate strain. *Geophysical Research Letters*, 39(5).
 459 <https://doi.org/10.1029/2011GL050712>
- 460 Ide, S., & Beroza, G. C. (2023). Slow earthquake scaling reconsidered as a boundary between distinct modes of
 461 rupture propagation. *Proceedings of the National Academy of Sciences of the United States of America*,
 462 120(32). <https://doi.org/10.1073/pnas.2222102120>
- 463 Igarashi, T., & Kato, A. (2021). Evolution of aseismic slip rate along plate boundary faults before and after
 464 megathrust earthquakes. *Communications Earth and Environment*, 2(1). <https://doi.org/10.1038/s43247-021-00127-5>
- 466 Im, K., Saffer, D., Marone, C., & Avouac, J. P. (2020). Slip-rate-dependent friction as a universal mechanism for
 467 slow slip events. *Nature Geoscience*, 13(10), 705–710. <https://doi.org/10.1038/s41561-020-0627-9>
- 468 Jara, J., Jolivet, R., Socquet, A., Comte, D., & Norabuena, E. (2024). Detection of slow slip events along the
 469 southern Peru - northern Chile subduction zone. *Seismica*, 3(1). <https://doi.org/10.26443/seismica.v3i1.980>
- 470 Jiang, Y., Liu, Z., Davis, E. E., Schwartz, S. Y., Dixon, T. H., Voss, N., et al. (2017). Strain release at the trench
 471 during shallow slow slip: The example of Nicoya Peninsula, Costa Rica. *Geophysical Research Letters*,
 472 44(10), 4846–4854. <https://doi.org/10.1002/2017GL072803>
- 473 Jolivet, R., & Frank, W. B. (2020). The transient and intermittent nature of slow slip. *AGU Advances*, 1(1).
 474 <https://doi.org/10.1029/2019av000126>
- 475 Kano, M., Aso, N., Matsuzawa, T., Ide, S., Annoura, S., Arai, R., et al. (2018). Development of a slow earthquake
 476 database. *Seismological Research Letters*, 89(4), 1566–1575. <https://doi.org/10.1785/0220180021>
- 477 Lallemand, S., & Heuret, A. (2017). Subduction Zones Parameters. *Reference Module in Earth Systems and*
 478 *Environmental Sciences*. <https://doi.org/10.1016/B978-0-12-409548-9.09495-1>
- 479 Lallemand, S., Peyret, M., van Rijsingen, E., Arcay, D., & Heuret, A. (2018). Roughness Characteristics of Oceanic
 480 Seafloor Prior to Subduction in Relation to the Seismogenic Potential of Subduction Zones. *Geochemistry,*
 481 *Geophysics, Geosystems*, 19(7), 2121–2146. <https://doi.org/10.1029/2018GC007434>
- 482 Lay, T., Kanamori, H., Ammon, C. J., Koper, K. D., Hutko, A. R., Ye, L., et al. (2012). Depth-varying rupture
 483 properties of subduction zone megathrust faults. *Journal of Geophysical Research: Solid Earth*, 117(4).
 484 <https://doi.org/10.1029/2011JB009133>
- 485 Li, & Liu, Y. (2016). Spatiotemporal evolution of slow slip events in a nonplanar fault model for northern Cascadia
 486 subduction zone. *Journal of Geophysical Research: Solid Earth*, 121(9), 6828–6845.
 487 <https://doi.org/10.1002/2016JB012857>
- 488 Locher, V. A., Bell, R. E., Salah, P., Platt, R., & John, C. M. (2025). Fingerprinting subduction margins using
 489 principal component analysis profiles: A data science approach to assessing earthquake hazard. *Geology*,
 490 53(5), 473–478. <https://doi.org/10.1130/G53056.1>
- 491 Lu, C., Grand, S. P., Lai, H., & Garnero, E. J. (2019). TX2019slab: A New P and S Tomography Model
 492 Incorporating Subducting Slabs. *Journal of Geophysical Research: Solid Earth*, 124(11), 11549–11567.
 493 <https://doi.org/10.1029/2019JB017448>
- 494 Lundberg, S. M., & Lee, S.-I. (2017). A Unified Approach to Interpreting Model Predictions. In *31st Conference on*
 495 *Neural Information Processing Systems (NIPS 2017)*. Long Beach, CA, USA.
- 496 McLellan, M., & Audet, P. (2020). Uncovering the physical controls of deep subduction zone slow slip using
 497 supervised classification of subducting plate features. *Geophysical Journal International*, 223(1), 94–110.
 498 <https://doi.org/10.1093/gji/ggaa285>

- 499 Mei, C., & Wang, L. (2024). Velocity Dependence of Rate-And-State Friction in Granular Fault Gouge and
 500 Implications for Slow-Slip Events. *Journal of Geophysical Research: Solid Earth*, 129(7).
 501 <https://doi.org/10.1029/2024JB029393>
- 502 Muldashev, I. A., & Sobolev, S. V. (2020). What Controls Maximum Magnitudes of Giant Subduction Earthquakes?
 503 *Geochemistry, Geophysics, Geosystems*, 21(9). <https://doi.org/10.1029/2020GC009145>
- 504 Münchmeyer, J., Molina-Ormazabal, D., Radiguet, M., Marsan, D., Baez, J. C., Ortega-Culaciati, F., et al. (2025).
 505 Seismic Swarms Unveil the Mechanisms Driving Shallow Slow Slip Dynamics in the Copiapó Ridge,
 506 Northern Chile. *Geophysical Research Letters*, 52(8). <https://doi.org/10.1029/2024GL113953>
- 507 Nishikawa, Ide, S., & Nishimura, T. (2023). A review on slow earthquakes in the Japan Trench. *Progress in Earth
 508 and Planetary Science*, 10(1). <https://doi.org/10.1186/s40645-022-00528-w>
- 509 Obara, K., & Kato, A. (2016). Connecting slow earthquakes to huge earthquakes. *Science*, 353 (6296), 253–257.
 510 <https://doi.org/10.1126/science.aaf1512>
- 511 Okada, Y., & Nishimura, T. (2025). Investigation on short-term slow slip events in the northeast Japan subduction
 512 zones using decadal GNSS data. *Earth, Planets and Space*, 77(1), 45. <https://doi.org/10.1186/s40623-025-02175-z>
- 514 Peng, Z., & Gomberg, J. (2010). An integrated perspective of the continuum between earthquakes and slow-slip
 515 phenomena. *Nature Geoscience*, 3(9), 599–607. <https://doi.org/10.1038/ngeo940>
- 516 Perez-Silva, A., Kaneko, Y., Savage, M., Wallace, L., Li, D., & Williams, C. (2022). Segmentation of Shallow Slow
 517 Slip Events at the Hikurangi Subduction Zone Explained by Along-Strike Changes in Fault Geometry and
 518 Plate Convergence Rates. *Journal of Geophysical Research: Solid Earth*, 127(1).
 519 <https://doi.org/10.1029/2021JB022913>
- 520 Perez-Silva, A., Kaneko, Y., Savage, M., Wallace, L., & Warren-Smith, E. (2023). Characteristics of Slow Slip
 521 Events Explained by Rate-Strengthening Faults Subject to Periodic Pore Fluid Pressure Changes. *Journal of
 522 Geophysical Research: Solid Earth*, 128(6). <https://doi.org/10.1029/2022JB026332>
- 523 Perry, M., Muller, C., Protti, M., Feng, L., & Hill, E. M. (2023). Shallow slow slip events identified offshore the Osa
 524 peninsula in southern Costa Rica from GNSS time series. *Geophysical Research Letters*, 50(20).
 525 <https://doi.org/10.1029/2023GL104771>
- 526 Plata-Martinez, R., Ide, S., Shinohara, M., Garcia, E. S., Mizuno, N., Dominguez, L. A., et al. (2021). Shallow slow
 527 earthquakes to decipher future catastrophic earthquakes in the Guerrero seismic gap. *Nature Communications*,
 528 12(1). <https://doi.org/10.1038/s41467-021-24210-9>
- 529 Probst, P., Boulesteix, A.-L., & Bischl, B. (2019). Tunability: Importance of Hyperparameters of Machine Learning
 530 Algorithms. *Journal of Machine Learning Research*, 20, 1–32.
- 531 Prokhorenkova, L., Gusev, G., Vorobev, A., Dorogush, A. V., & Gulin, A. (2018). CatBoost: unbiased boosting
 532 with categorical features. In *32nd Conference on Neural Information Processing Systems (NeurIPS)*.
 533 Montréal, Canada.
- 534 Sáez, M., Ruiz, S., Ide, S., & Sugioka, H. (2019). Shallow nonvolcanic tremor activity and potential repeating
 535 earthquakes in the Chile triple junction: Seismic evidence of the subduction of the active Nazca–Antarctic
 536 spreading center. *Seismological Research Letters*, 90(5), 1740–1747. <https://doi.org/10.1785/0220180394>
- 537 Saffer, D. M., & Wallace, L. M. (2015). The frictional, hydrologic, metamorphic and thermal habitat of shallow
 538 slow earthquakes. *Nature Geoscience*, 8(8), 594–600. <https://doi.org/10.1038/ngeo2490>
- 539 Shreedharan, S., Ikari, M., Wood, C., Saffer, D., Wallace, L., & Marone, C. (2022). Frictional and Lithological
 540 Controls on Shallow Slow Slip at the Northern Hikurangi Margin. *Geochemistry, Geophysics, Geosystems*,
 541 23(2). <https://doi.org/10.1029/2021GC010107>
- 542 Socquet, A., Valdes, J. P., Jara, J., Cotton, F., Walpersdorf, A., Cotte, N., et al. (2017). An 8 month slow slip event
 543 triggers progressive nucleation of the 2014 Chile megathrust. *Geophysical Research Letters*, 44(9), 4046–
 544 4053. <https://doi.org/10.1002/2017GL073023>
- 545 Wada, I., & Wang, K. (2009). Common depth of slab-mantle decoupling: Reconciling diversity and uniformity of
 546 subduction zones. *Geochemistry, Geophysics, Geosystems*, 10(10). <https://doi.org/10.1029/2009GC002570>
- 547 Wallace, L., Beavan, J., Bannister, S., & Williams, C. (2012). Simultaneous long-term and short-term slow slip
 548 events at the Hikurangi subduction margin, New Zealand: Implications for processes that control slow slip
 549 event occurrence, duration, and migration. *Journal of Geophysical Research: Solid Earth*, 117(11).
 550 <https://doi.org/10.1029/2012JB009489>
- 551 Wallace, L., Webb, S., Ito, Y., Mochizuko, K., Hino, R., Henrys, S., et al. (2016). Slow slip near the trench at the
 552 Hikurangi subduction zone, New Zealand. *Science*, 352(6286), 697–701.
 553 <https://doi.org/10.1126/science.aad9521>

- 554 Wang, K., & Bilek, S. L. (2014). Fault creep caused by subduction of rough seafloor relief. *Tectonophysics*, 610, 1–
 555 24. <https://doi.org/10.1016/j.tecto.2013.11.024>
- 556 Zou, M., Jiang, W. G., Qin, Q. H., Liu, Y. C., & Li, M. L. (2022). Optimized XGBoost Model with Small Dataset
 557 for Predicting Relative Density of Ti-6Al-4V Parts Manufactured by Selective Laser Melting. *Materials*,
 558 15(5298). <https://doi.org/10.3390/ma15155298>
 559

560 **References from the Supporting Information**

- 561 Altamimi, Z., Rebischung, P., Collilieux, X., Métivier, L., & Chanard, K. (2023). ITRF2020: an augmented reference
 562 frame refining the modeling of nonlinear station motions. *Journal of Geodesy*, 97(5).
 563 <https://doi.org/10.1007/s00190-023-01738-w>
- 564 Ferrer, L. (2023). Analysis and Comparison of Classification Metrics. <http://arxiv.org/abs/2209.05355>
- 565 GEBCO Bathymetric Compilation Group. (2024). The GEBCO_2024 Grid - a continuous terrain model of the global
 566 oceans and land. 2024. <https://doi.org/doi:10.5285/1c44ce99-0a0d-5f4f-e063-7086abc0ea0f>
- 567 Hernández-Orallo, J., Flach, P., & Ferri, C. (2012). Threshold choice methods: the missing link.
 568 <https://doi.org/10.48550/arXiv.1112.2640>
- 569 Mooney, W. D., Barrera-Lopez, C., Suárez, M. G., & Castelblanco, M. A. (2023). Earth Crustal Model 1 (ECM1): A
 570 1° x 1° global seismic and density model. *Earth-Science Reviews*, 243.
 571 <https://doi.org/10.1016/j.earscirev.2023.104493>
- 572 Müller, R. D., Seton, M., Zahirovic, S., Williams, S. E., Matthews, K. J., Wright, N. M., Shephard, G. E., Maloney,
 573 K. T., Barnett-Moore, N., Hosseinpour, M., Bower, D. J., & Cannon, J. (2016). Ocean Basin Evolution and
 574 Global-Scale Plate Reorganization Events since Pangea Breakup. *Annual Review of Earth and Planetary
 575 Sciences*, 44, 107–138. <https://doi.org/10.1146/annurev-earth-060115-012211>
- 576 Seton, M., Müller, R. D., Zahirovic, S., Williams, S. E., Cannon, J., Seton, M., Bower, D. J., Tetley, M. G., Heine, C.,
 577 Le Breton, E., Liu, S., Russell, S. H. J., Yang, T., Leonard, J., & Gurnis, M. (2020). A global data set of present-
 578 day oceanic crustal age and seafloor spreading parameters. *Geochemistry, Geophysics, Geosystems*, 21.
 579 <https://doi.org/10.1029/2020GC009214>
- 580 UNAVCO. (2025). Plate Motion Calculator. UNAVCO, Inc. [https://www.unavco.org/software/geodetic-
 581 utilities/plate-motion-calculator/plate-motion-calculator.html](https://www.unavco.org/software/geodetic-utilities/plate-motion-calculator/plate-motion-calculator.html)
- 582